Advanced Fiber Materials (2022) 4:820–831
https://doi.org/10.1007/s42765-022-00140-z

RESEARCH ARTICLE

Compressible and Lightweight MXene/Carbon Nanofiber Aerogel with "Layer-Strut" Bracing Microscopic Architecture for Efficient Energy Storage

Yongpeng Liu[1] · **Dan Wang**[1] · **Chao Zhang**[2] · **Yan Zhao**[3] · **Piming Ma**[1] · **Weifu Dong**[1] · **Yunpeng Huang**[1] · **Tianxi Liu**[1]

Received: 22 October 2021 / Accepted: 23 January 2022 / Published online: 4 March 2022

Abstract

Two-dimensional MXene has recently captured widespread research attention in energy storage and conversion fields due to its high conductivity, large specific surface area, and remarkable electro-activity. However, its performance is still hindered by severe self-restacking of MXene flakes. Herein, conductive $Ti_3C_2T_x$/carbon nanofiber (CNF) composite aerogel with typical "layer-strut" bracing 3D microscopic architecture has been fabricated via synergistic assembly and freeze-drying process. In virtu of the strong interfacial interaction between polymeric precursor nanofibers and MXene mono-layers, gelation capability and 3D formability of $Ti_3C_2T_x$ is greatly reinforced, as resulted $Ti_3C_2T_x$/CNF aerogels possess a highly ordered microporous structure with interlayered CNF penetrating between large size MXene lamellae. This special configuration guarantees the stability and pliability of the composite aerogels. Furthermore, the 3D form interconnected conductive network and the parallell alignment of the pores allow free electrical carriers motion and ion migration. As a result, the prepared $Ti_3C_2T_x$/CNF aerogel-based electrode exhibits an exceptional gravimetric specific capacitance of 268 F g^{-1} at a current density of 0.5 A g^{-1} and an excellent cycling stability of 8000 cylcles, and the assembled symmetric supercapacitor, delivers a high energy density of 3.425 W h kg^{-1} at 6000 W kg^{-1}. This work offers a new route for the rational construction of 3D MXene assembly for advanced energy storage materials.

Keywords MXene · Electrospinning · Aerogels · Layered microstructures · Energy storage

---

✉ Yunpeng Huang
hypjnu@jiangnan.edu.cn

✉ Tianxi Liu
txliu@jiangnan.edu.cn

[1] Key Laboratory of Synthetic and Biological Colloids, School of Chemical and Material Engineering, Ministry of Education, Jiangnan University, Wuxi 214122, China

[2] State Key Laboratory for Modification of Chemical Fibers and Polymer Materials, College of Materials Science and Engineering, Donghua University, Shanghai 201620, China

[3] School of Resources, Environment and Materials, Guangxi University, Nanning 530004, China

Introduction

Advancing of portable electronics fueled a revolutionary development of flexible and high-power density storage systems. Compared with other energy storage systems, supercapacitors (SCs) offer the advantages of fast charging and discharging speed, high power density, and reliable cycle life, thus have recently attracted excessive attention for rapid discharge applications [1–5]. Generally, the energy storage in supercapacitors is based on two principles: (1) electric double layer capacitance (EDLC) due to the electrostatic separation of charges at the interface, between electrode and electrolyte without faradaic reactions; (2) pseudocapacitance due to the faradaic reactions, intercalation, or electrosorption at or near the surface of electrode materials. Carbon materials are currently the most popular electrode materials for EDLC, including but not limited to fullerenes, carbon nanotubes, carbon fiber, graphene, and conductive carbon black. Although carbon materials possess the decent capacity and cycling stability, their energy density and power density are relatively low. Pseudocapacitive materials including metal oxides/sulfides [6], hydroxides [7, 8], and conductive conjugated polymers [9, 10] always exhibit high specific capacity and energy/power densities, while their cycling performance is still poor. Hence, developing the new electrodes for flexible and high-performance supercapacitors with a simple and cost-effective approach is highly demanded.

MXene is a rising star among two-dimensional (2D) nanomaterials with the general formula $M_{n+1}X_nT_x$ (n = 1–3), where represents an early transition metal, X stands for carbon and/or nitrogen, and T stands for the exposed surface terminations, including hydroxyl (–OH), oxygen (–O), and fluorine (–F) groups. Owing to it's distinctive composition and structure, MXene has found tremendous new applications in energy storage and conversion [11, 12], electromagnetic shielding and absorption [13, 14], sensors and actuators [15, 16] and so on [17–19]. In particular, MXene specimens demonstrate various superior chemical/physical properties including high metallic conductivity, large specific surface area, and strong mechanical strength, endowing MXene with promising performance in energy storage applications. However, MXene nanosheets potentially undertakes irreversible restacking or spontaneously collapse, due to the strong Van der Waals interactions between individual layers, originated from their 2D nano-structure [20]. These structural deformation greatly reduces the specific surface area of the MXene-based electrode materials, and severely constrains the diffusion speed and intercalation efficiency of the electrolyte ions in the MXene electrodes. In addition to the limited ion transport in pyknotic structures, the conductivity of electrons between multiple-layered MXene is largely hindered by anisotropic nature of MXene flakes. There are two main strategies to solve these problems; one is to introduce intercalators, such as carbon nanotubes, graphene oxides [21, 22], conducting polymers, etc. [23, 24], to prevent MXene mono-layer from re-stacking. A more promising approach is to engineer the structure of MXene, to construct a porous three-dimensional macroscopic lattice [25, 26]. Nonetheless, the 3D assembly of MXene with both structural integrity and excellent electrochemical properties currently remains a great challenge due to the poor gelation ability of MXene flakes [27].

In this work, a $Ti_3C_2T_x$/CNF composite aerogel with typical "layer-strut" bracing 3D microscopic architecture is prepared by the synergistic assembly and freeze-drying process utilizing the shortened polyacrylonitrile (PAN) nanofibers as crosslinking and intercalating building blocks. Based on the strong interfacial interaction between 2D $Ti_3C_2T_x$ flakes and polymeric PAN fibers, the gelation capability and 3D formability of $Ti_3C_2T_x$ is greatly improved, resulting in a robust and pliable $Ti_3C_2T_x$/CNF composite aerogels with highly ordered microporous structure composed of CNF, penetrating between large size MXene lamellae. The special "layer-strut" bracing 3D microscopic structure provides convenient channels for electron transport and ion migration, hence, the $Ti_3C_2T_x$/CNF electrode exhibits an outstanding gravimetric specific capacitance of 268 F g^{-1} at a current density of 0.5 A g^{-1}, and excellent cycling stability of 8000 cycles. Moreover, the fabricated $Ti_3C_2T_x$/CNF symmetric supercapacitor device even delivers a high energy density of 3.425 W h kg^{-1} at 6000 W kg^{-1} together with excellent cycling stability. Therefore, this work may provide a promising approach for the development of robust MXene assemblies for high-performance electrode material.

Experimental Section

Materials

Polyacrylonitrile (PAN, Mw = 150,000 g mol^{-1}) was purchased from Sigma-Aldrich. Ti_3AlC_2 (400 mesh) was bought from 11 technology, co., Ltd. Hydrochloric acid (HCl, 36–38%) and *N,N*-dimethylformamide (DMF) were obtained from Sinopharm Chemical Reagent Co., Ltd. Lithium fluoride (LiF) was provided by Aladdin Reagent Company.

Fabrication of Shortened PAN Nanofibers

In a typical process, 1 g PAN powder was dissolved in 10 mL DMF under vigorous stirring in an 80 °C oil bath. Afterward, electrospinning was carried out on a commercial electrospinning system (UCALERY Beijing Co., LTD, China) at an applied voltage of 15–18 kV, the feeding speed and orifice to collector distance were set as 2.5 mL h^{-1} and 15 cm, respectively. Obtained free-standing PAN nanofiber web was pre-oxidized in the air under 250 °C for 2 h, followed by the homogenization process under 10,000 rpm for 30 min to obtain shortened PAN nanofibers.

Synthesis of $Ti_3C_2T_x$ MXene

The mono-layered $Ti_3C_2T_x$ MXene was prepared by etching MAX phase Ti_3AlC_2 with LiF and HCl. Briefly, 2 g LiF was first dissolved in 30 mL HCl (9 mol L^{-1}) under vigorous stirring for 20 min, 1 g Ti_3AlC_2 was then slowly added into the mixed solution, followed by reaction at 35 °C under mild stirring for 24 h, resulted black product was washed with DI water for 7–8 times until the pH of the supernatant beyond 6. The remained sediment of multi-layered MXene was then exfoliated under 240 W ultrasonication for 60 min under the protection of N_2 and ice bath. Mono-layered $Ti_3C_2T_x$ powder was acquired by freeze-drying and preserved by vacuum packing.

Preparation of $Ti_3C_2T_x$/CNF Composite Aerogel

To begin with, $Ti_3C_2T_x$ powder was dispersed in deionized water under ultrasonication, for 30 min to prepare stable MXene suspension, shortened PAN nanofibers were then added to the above suspension and treated with magnetic stirring to obtain the homogeneously mixed dispersion with different $Ti_3C_2T_x$/PAN mass ratios (6:2, 4:4, and 2:6). After 24 h gelation and assembly under mild stirring, 10 mL of the above mixture was transferred to cylindrical moulds and freezing in a − 90 °C ethanol refrigerant, followed by freeze-drying in a lyophilizer (− 80 °C, 0.1 mbar) for 72 h to achieve $Ti_3C_2T_x$/PAN aerogels, which were further carbonized at 100 °C for 1 h and 600 °C in H_2/Ar for 1 h to obtain $Ti_3C_2T_x$/CNF composite aerogels. For comparison, pure PAN nanofiber assembly was also prepared by freeze-drying under the same conditions.

Materials Characterization

Morphologies of the assembled composites were evaluated by field emission scanning electron microscope (FESEM, Hitachi, S4800). TEM images were captured using a JEM-2100 plus transmission electron microscope (Japan). AFM images were obtained using a MultiMode 8 system from Bruker. XRD measurement was conducted on a Bruker D8 X-ray diffractometer with a Cu Kα X-ray source (λ = 1.5418 Å). XPS was carried out on ESCA 2000 (VG Microtech, UK) using a monochromic Al Ka (hn ¼ 1486.6 eV) X-ray source.

Electrochemical Measurements

During three-electrode electrochemical tests, self-supported aerogels pressed on the nickel foam were directly used as the binder-free working electrodes. All the electrochemical experiments, including cyclic voltammetry (CV), galvanostatic charge–discharge (GCD), and electrochemical impedance spectroscopy (EIS) measurements were performed on a Gamry Interface 5000P workstation (Gamry Instruments, America) to evaluate their electrochemical performance. Pt plate and Ag/AgCl electrodes were used as the counter electrode and the reference electrode. The gravimetric specific capacitance (C, F g^{-1}) and capacity (Q, C g^{-1}) were calculated from their discharge curves according to the following equations:

$$C = \frac{\mathrm{I\Delta t}}{\mathrm{m\Delta V}} \tag{1}$$

$$Q = \frac{\mathrm{I\Delta t}}{\mathrm{m}} \tag{2}$$

where I is the discharge current (A), Δt is the discharge time (s), m is the mass loadings of the working electrode (g), and ΔV is the discharge voltage (V).

The symmetric supercapacitor device was assembled using the self-supported $Ti_3C_2T_x$/CNF composite aerogel as the positive electrode and the negative electrode, a 1 M H_2SO_4 solution was used as electrolyte, and a cellulose paper as the separator (obtained device was named as $Ti_3C_2T_x$/CNF//$Ti_3C_2T_x$/CNF SSCs).

The mass-specific energy density (E, W h kg^{-1}) and power density (P, W kg^{-1}) of the SSCs device were calculated using the following equations:

$$\mathrm{E} = \frac{1}{2}\mathrm{CV}^2 \tag{3}$$

$$\mathrm{P} = \frac{\mathrm{E}}{\Delta}\mathrm{t} \tag{4}$$

where C is the gravimetric specific capacitance (F g^{-1}), V is the discharge voltage (V), and Δt is the discharge time (s).

Results and Discussion

Figure 1 schematically illustrates the fabrication process of $Ti_3C_2T_x$/CNF composite aerogel. Through etching and exfoliation of the Ti_3AlC_2 (MAX), mono-layered $Ti_3C_2T_x$ MXene dispersion with obvious Tyndall effect can be observed in Fig. 2A. It is well-known that the removal of Al atoms in Ti_3AlC_2 can result in substantial surface-active

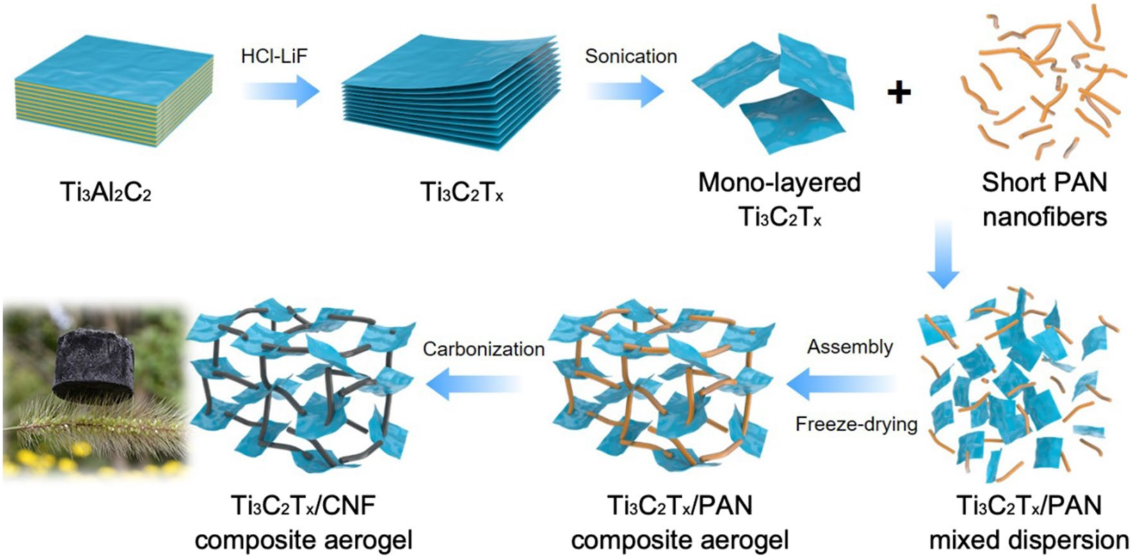

Fig. 1 Schematic illustration of the fabrication process of $Ti_3C_2T_x$/CNF composite aerogel

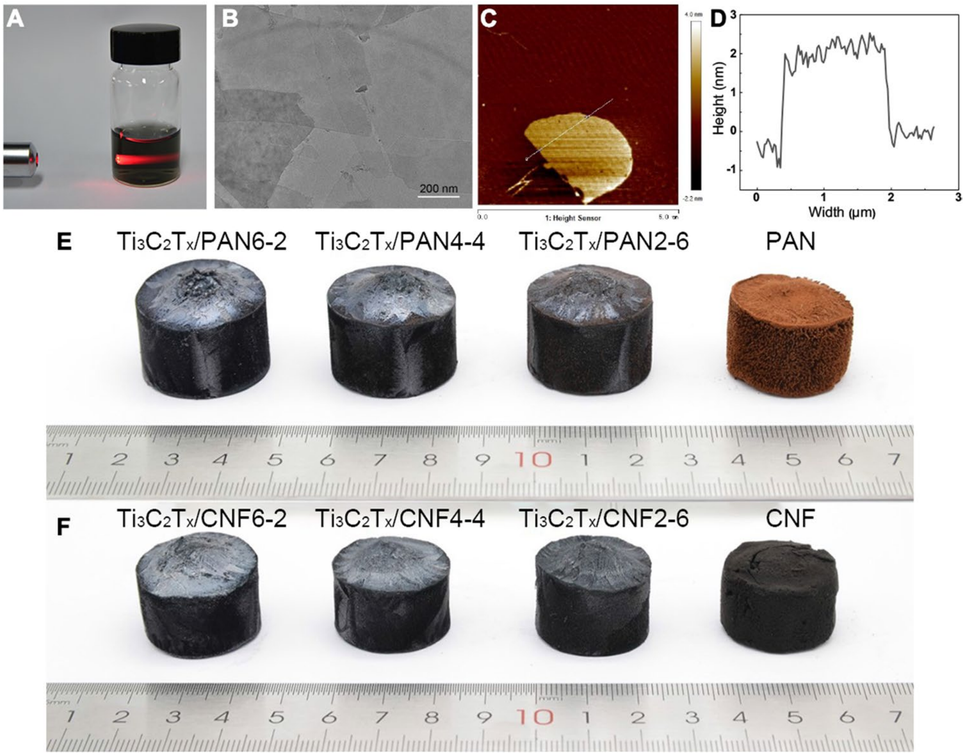

Fig. 2 **A** Digital photo of as-prepared MXene aqueous dispersion. **B**–**D** TEM and AFM images of synthesized $Ti_2C_2T_x$ MXene. **E**, **F** Digital photographs of prepared aerogels before and after thermal treatment

groups (e.g. –F, –O, and –OH) on MXene, thus potentially improves the interfacial interaction between MXene and polymeric nanofibers. TEM, AFM images, and corresponding height distribution in Fig. 2B, D show that the obtained $Ti_3C_2T_x$ MXene has a lateral size of about 1 um and a thickness of about 2.5 nm, implying the mono-layered structure of prepared MXene. Freshly-prepared electrospun PAN nanofibers treated with high-speed homogenization

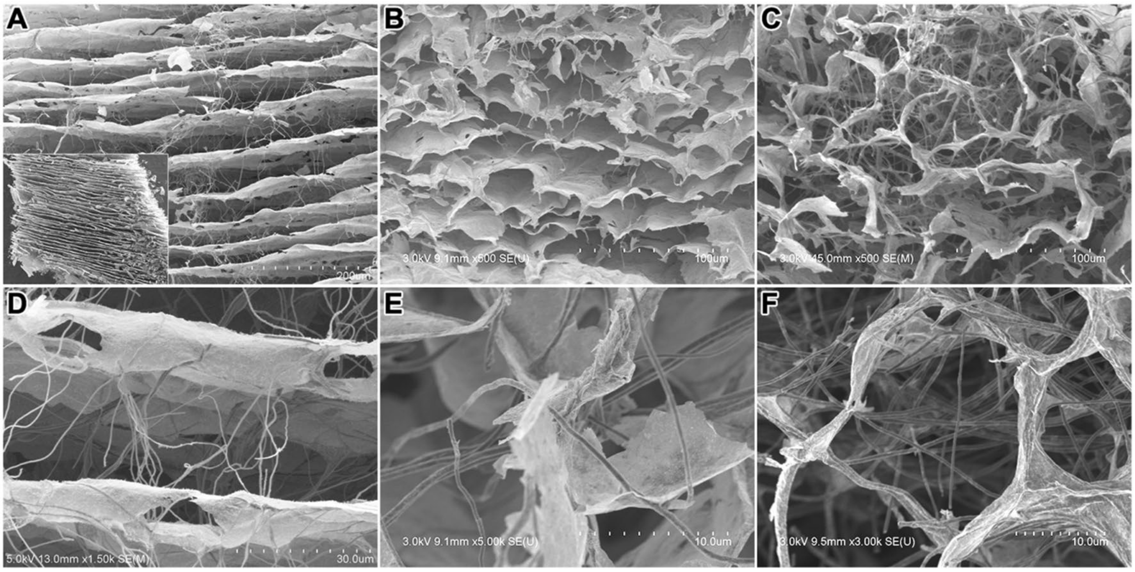

Fig. 3 SEM images of **A**, **D** $Ti_3C_2T_x$/CNF6-2, **B**, **E** $Ti_3C_2T_x$/CNF4-4, and **C**, **F** $Ti_3C_2T_x$/CNF2-6 aerogels at different magnifications

possess a homogeneous length distribution of 40–60 μm (Figure S1A), which can be well dispersed in water due to the numerous hydrophilic groups on the PAN fiber (Figure S1B). The excellent aqueous processability of shortened PAN fibers will facilitate their subsequent hybridization and gelation with MXene flakes.

The lamellar $Ti_3C_2T_x$ dispersion and pre-oxidized PAN short fibers were mixed and assembled with different $Ti_3C_2T_x$:PAN mass ratios, followed by freeze-drying and carbonization to obtain macroscopic aerogels. As displayed in Fig. 2E, $Ti_3C_2T_x$/PAN aerogels with different mass ratios all show excellent formability with no cracks and collapse on the monoliths, contrarily, numerous holes and voids can be clearly observed by naked eyes in pure PAN assembly, demonstrating the superior gelation between $Ti_3C_2T_x$ flakes and short PAN fibers. After carbonization at argon atmosphere, to convert polymeric nanofibers into carbon nanofibers and producing the $Ti_3C_2T_x$/CNF aerogels, all samples appear with shirankage (Fig. 2F), which is ascribed to decomposition of polymers and formation of cylindrical pores. It is notable that the carbonized PAN monolith shows conspicuous cracks, which highly contribute in superior structural stability of the Ti_{32x} composite aerogels.

The microstructures of different aerogels, i.e., $Ti_3C_2T_x$/CNF6-2, $Ti_3C_2T_x$/CNF4-4, and $Ti_3C_2T_x$/CNF2-6 were assessed by SEM. As shown in Fig. 3A, D, $Ti_3C_2T_x$/CNF6-2 composite aerogel manifests a "layer-strut" bracing 3D microscopic architecture with carbon nanofibers intercalating between parallelly aligned MXene flakes. It can be inferred that the CNF strut can largely improve the mechanical performance of the composite aerogels by absorbing the external loading, as well as facilitating the efficient charge transfer through the inter-connected conducting networks. It is also worth mentioning that the voids and porosity in the microscopic architecture are highly beneficial for the fast transportation of electrolyte ions. Hence, this special "layer-strut" bracing 3D microporous structure holds great potential in the application of energy storage applications. Further increasing of the mass ratio of carbon nanofibers, this is the main reason of disordered porous structures of the composite aerogels. Based on Fig. 3, the parallel structures can hardly be observed in $Ti_3C_2T_x$/CNF4-4 (Fig. 3B, E) and $Ti_3C_2T_x$/CNF2-6 (Fig. 3C, F) samples due to the significantly decreased amount of MXene flakes. Absence of the "layer-strut" bracing 3D microporous structure in the latter two aerogels potentially degrade their mechanical and electrochemical properties. However, intimate bindings between MXene and nanofibers can be identified in all samples (Fig. 3D, F), the tight connection derived from the strong interfacial interaction between PAN and $Ti_3C_2T_x$ can ensure the great structural integrity and mechanical strength of the composite aerogels. Homogenized electrospun PAN nanofibers were also freeze-dried and carbonized as presented in Fig. 2, obtained CNF assembly is constructed by randomly inter-weaved short nanofibers without any bindings between fibers (Figure S2). The cracks in CNF block are mainly created by this specific morphology. It is worth to mention that assemblies with higher MXene content manifest poor formability due to the lack of sufficient CNF supporting building blocks.

The crystal structures of different samples were characterized using wide-angle X-ray diffraction (XRD). As illustrated in Fig. 4A, pure $Ti_3C_2T_x$ powder and $Ti_3C_2T_x$/CNF aerogels all reveal the characteristic 002 crystal plane of

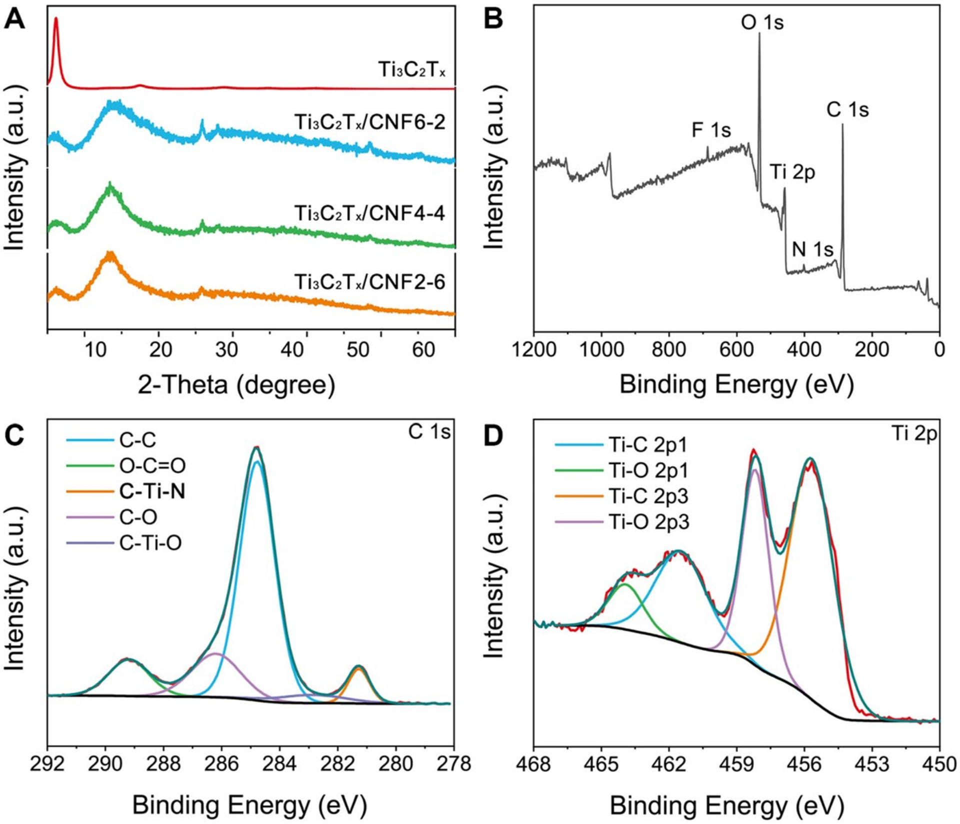

Fig. 4 **A** XRD patterns of $Ti_3C_2T_x$ and different $Ti_3C_2T_x$/CNF aerogels. **B** Survey spectrum, **C** C 1s and **D** Ti 2p spectra of $Ti_3C_2T_x$/CNF6-2 aerogel

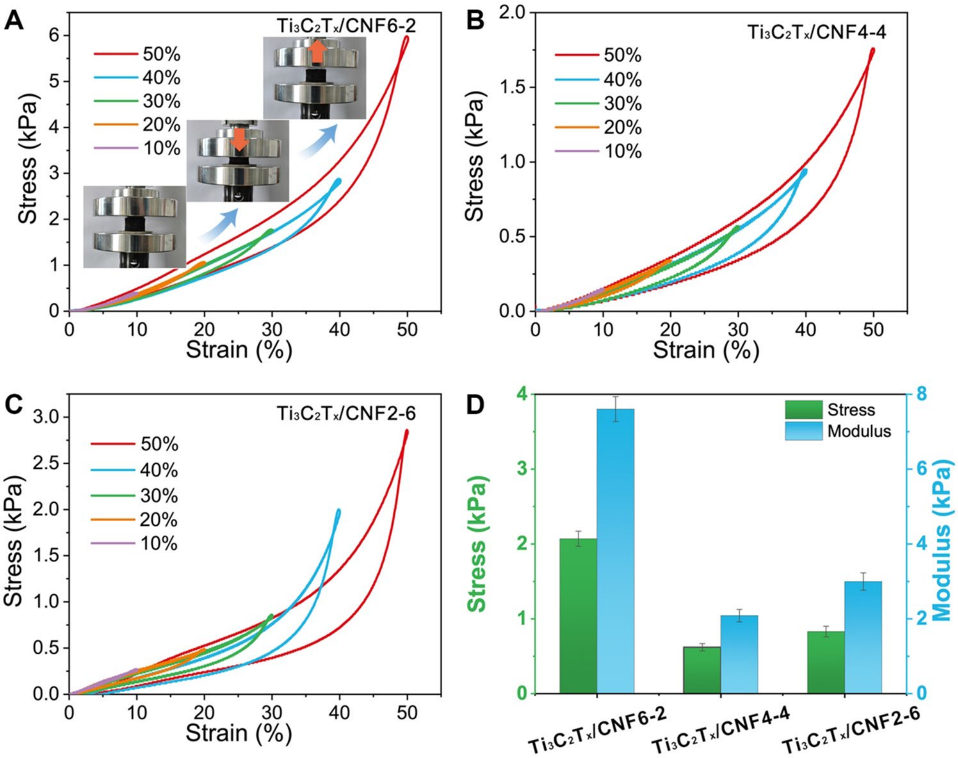

Fig. 5 The stress-strain curves of **A** $Ti_3C_2T_x$/CNF6-2, **B** $Ti_3C_2T_x$/CNF4-4, and **C** $Ti_3C_2T_x$/CNF2-6 composite aerogel upon various strains. **D** Comparison on the compressive modulus and strength between different samples. Inset of **A** is the photographs of aerogel at original, compressed and released state

$Ti_3C_2T_x$ at about 6.5°. However, the intensity of the 002 diffraction peak of $Ti_3C_2T_x$/CNF aerogels becomes weaker and their half-peak width also increases, which is caused by the hybridization of the two building blocks. Meanwhile, all $Ti_3C_2T_x$/CNF aerogels display the obvious amorphous carbon peaks at 14°, indicating the complete carbonization of polymeric nanofibers after sintering under Ar/H_2 atmosphere. Notably, other inconspicuous diffraction peaks at 26° and 57° can be indexed to the TiO_2 formed from the inevitable oxidation of Ti in $Ti_3C_2T_x$ during the carbonization process. XPS analysis was employed to further understand the chemical composition of $Ti_3C_2T_x$/CNF composite aerogel. As shown in Fig. 4B, the survey spectrum of $Ti_3C_2T_x$/CNF6-2 displays the elemental peaks of C, Ti, O, F, and N, corresponding to the composition of MXene and residual nitrogen in CNF after thermal decomposition of PAN. Bonding states of C 1s were further analyzed at high resolution, as shown in Fig. 4C, the appearance of C–Ti–N clearly indicates the chemical interaction between CNF and MXene building blocks. It is worth noting that, the high-resolution Ti 2p spectra of MXene present a sharp Ti–O peak at a binding energy of 458.3 eV (Fig. 4D), revealing the oxidation of $Ti_3C_2T_x$ during high-temperature treatment, in accordance with the XRD results.

Aerogel electrode materials are of great interest because of their compressibility and flexibility. Here, a series of compression tests were conducted at a compression rate of 10 mm min^{-1} to study the mechanical properties of $Ti_3C_2T_x$/CNF6-2, $Ti_3C_2T_x$/CNF4-4, and $Ti_3C_2T_x$/CNF2-6 composite aerogels. As shown in Fig. 5A–D, $Ti_3C_2T_x$/CNF6-2 displays the highest stress at 50% compressive strain. Contrarily, $Ti_3C_2T_x$/CNF2-6 and $Ti_3C_2T_x$/CNF4-4 counterparts can only withstand lower stress and show lower modulus. Specifically, two different stages can be clearly observed during the loading process of all $Ti_3C_2T_x$/CNF composite aerogel under different strains. The first linear part is below 40% strain corresponding to the elastic region of the aerogels, when the stress increases gradually with a relatively lower speed due to the slow compression of large size pores. Following that, a sharp increase in the stress at higher strain (beyond 40%) can be identified arising from the tight contact between building blocks in the composite aerogels (as shown in Fig. 3). The superior mechanical properties of $Ti_3C_2T_x$/CNF6-2 is definitely stem from its special "layer-strut" bracing 3D microscopic architecture, where carbon nanofibers intercalating between parallelly aligned MXene flakes can function as struts to withstand large-scale deformation and rebound to their initial state after unloading. The lower modulus and strength manifested by $Ti_3C_2T_x$/CNF4-4 compared with $Ti_3C_2T_x$/CNF2-6 can be ascribed to the structural difference between two samples (Fig. 5D). $Ti_3C_2T_x$/CNF2-6 contains more CNF, which serve as supporting building blocks to assure higher rigidity, thus results in the better mechanical properties of $Ti_3C_2T_x$/CNF2-6.

The electrochemical properties of as-prepared electrodes were evaluated in three-electrode cells by directly using the

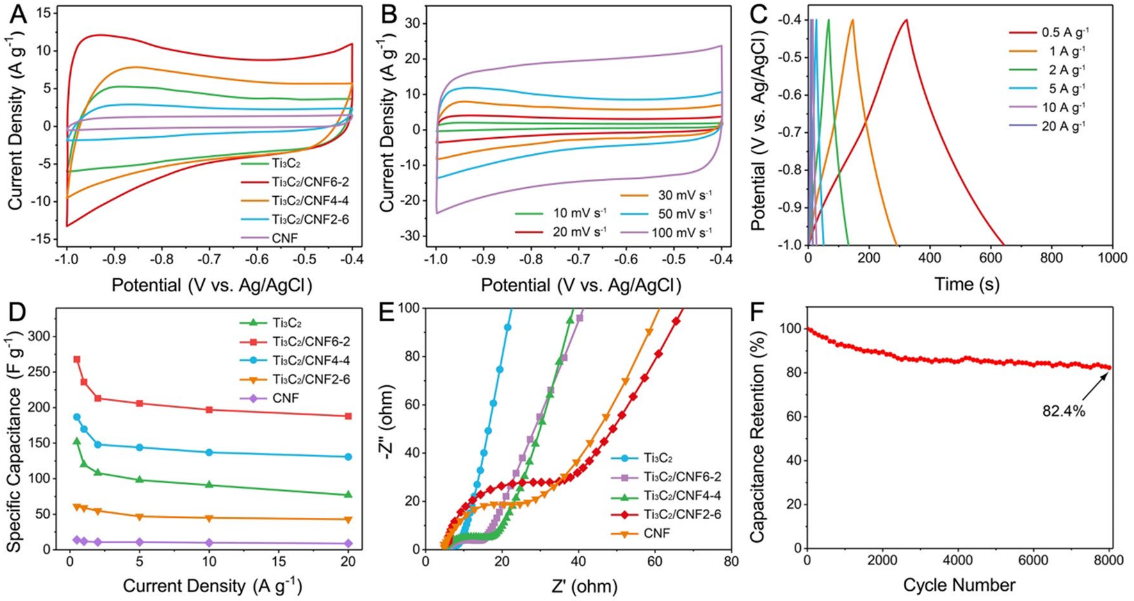

Fig. 6 Electrochemical performance of different electrodes. **A** CV curves of $Ti_3C_2T_x$, $Ti_3C_2T_x$/CNF6-2, $Ti_3C_2T_x$/CNF4-4, $Ti_3C_2T_x$/CNF2-6, CNF electrodes at a scan rate of 50 mV s^{-1}. **B** CV curves of the $Ti_3C_2T_x$/CNF6-2 aerogel electrode at different scan rates. **C** Charge–discharge curves of the $Ti_3C_2T_x$/CNF6-2 aerogel electrode at various current densities. **D** Specific capacitance of different electrodes at various current densities. **E** EIS analysis of different electrodes in 1 M H_2SO_4 electrolyte. **F** Cycling stability of $Ti_3C_2T_x$/CNF6-2 aerogel electrode at a current density of 1 A g^{-1}

self-supported composite aerogels as binder-free working electrodes. Figure 6 A shows the CV profiles of pure $Ti_3C_2T_x$, pure CNF, $Ti_3C_2T_x$/CNF6-2, $Ti_3C_2T_x$/CNF4-4, and $Ti_3C_2T_x$/CNF2-6 composite aerogels, recorded in a potential window of − 1.0 to − 0.4 V, with a scan rate of 50 mV s^{-1}. Obvious double-layer capacitive behavior can be confirmed for all electrodes by presenting near rectangular shapes of their CV curves. Out of the examined samples $Ti_3C_2T_x$/CNF6-2 and $Ti_3C_2T_x$/CNF4-4 composite electrodes manifest larger CV area than other electrodes, indicating the superior capacitive performance of the composite aerogel, which is possibly ascribed to the greatly improved surface area and fast charge transfer paths constructed by few-layered $Ti_3C_2T_x$ sheets and CNF nanofibers. It is remarkable that $Ti_3C_2T_x$/CNF2-6 possesses inferior capacitive performance compared with pure Ti_3C_2. This might be due to the dominance of amorphous carbon in this electrode. It is also notable that $Ti_3C_2T_x$/CNF6-2 exhibits the best capacitive performance among three aerogels, indicating the well-defined "layer-strut" bracing 3D microscopic architecture of $Ti_3C_2T_x$/CNF6-2 can effectively enhance its electrochemical properties. Furthermore, the CV curves of the $Ti_3C_2T_x$/CNF6-2 composite electrode at different scan rates ranging from 10 to 100 mV s^{-1} are presented in Fig. 6B, from which the area of the CV curves can be observed increasing with the increase of the scan rate. Galvanostatic charge–discharge (GCD) tests were further conducted to determine the capacitive performance of the $Ti_3C_2T_x$/CNF6-2 composite electrode. As revealed in Fig. 6C, the GCD curves of the $Ti_3C_2T_x$/CNF6-2 electrode at various current densities within the potential window of − 1.0 to − 0.4 V, show the typical triangular configuration, confirming the characteristics of electric double-layer capacitors (EDLC). The well-symmetric GCD curves also suggest a reversible capacity and an excellent coulombic efficiency of the electrodes. The GCD curve of $Ti_3C_2T_x$/CNF4-4, $Ti_3C_2T_x$/CNF2-6, $Ti_3C_2T_{x,}$ and CNF (Figure S3A–3D) also exhibit a similar trend. According to the GCD results, the specific capacitances of the three electrodes are calculated based on Eq. (1). Figure 6D presents the specific capacitance versus discharge current density for all prepared electrodes, the gravimetric specific capacitance of the $Ti_3C_2T_x$/CNF6-2 electrode reaches 268 F g^{-1} (161 C g^{-1}) at 0.5 A g^{-1}, which is the highest among $Ti_3C_2T_x$/CNF4-4 (187 F g^{-1} (112 C g^{-1})), $Ti_3C_2T_x$/CNF2-6 (61 F g^{-1} (37 C g^{-1})), $Ti_3C_2T_x$ (152 F g^{-1} (91 C g^{-1})) and CNF (14 F g^{-1} (8 C g^{-1})) electrodes. Note that the specific capacitance of the $Ti_3C_2T_x$/CNF6-2 electrode still remains 200 F g^{-1} at a high current density of 20 A g^{-1}, demonstrating the excellent rate capability of the aerogel electrode.

Electrochemical impedance spectroscopy (EIS) was performed at the open-circuit potential to further assess the

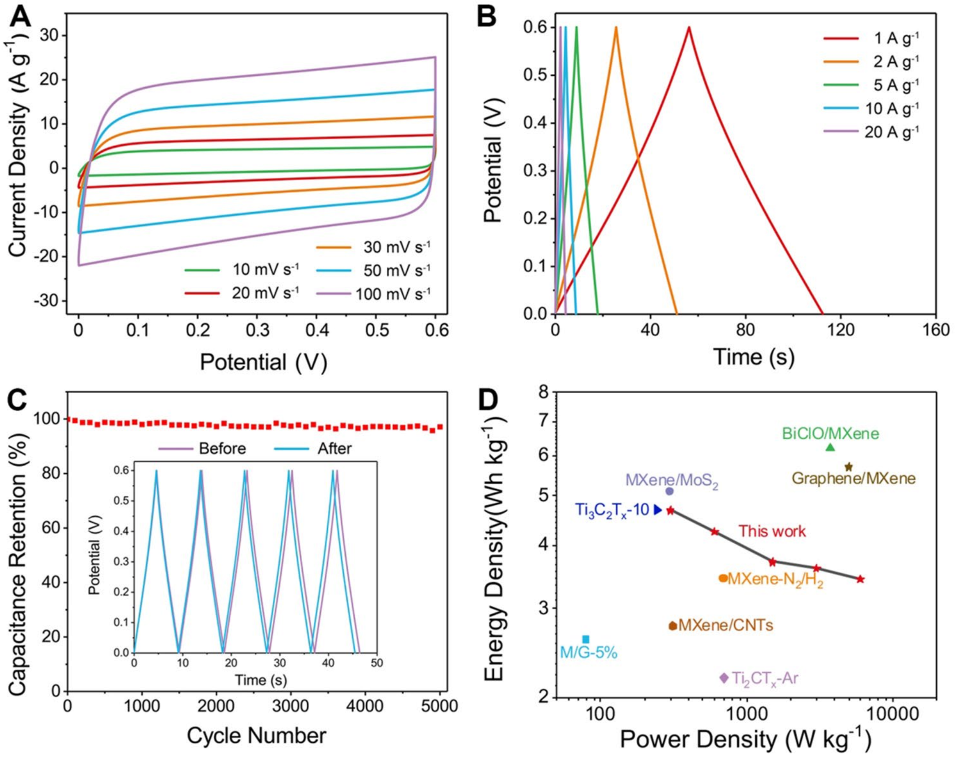

Fig. 7 Capacitive performance of $Ti_3C_2T_x$/CNF6-2//$Ti_3C_2T_x$/CNF6-2 SSC. **A** CV curves at different scan rates. **B** Charge–discharge curves of at various current densities. **C** Plot showing the variation of capacity retention under cycling test (inset shows the first and last five charge–discharge curves). **D** Ragone plots of the assembled SSC device

electrochemical performance of the electrodes in a frequency range of 0.01–100 kHz. As shown in the obtained Nyquist plots (Fig. 6E), the intercept in high-frequency region corresponds to the intrinsic series resistance (R_s) within the electrode. The R_s of $Ti_3C_2T_x$/CNF6-2, $Ti_3C_2T_x$/CNF4-4, $Ti_3C_2T_x$/CNF2-6, $Ti_3C_2T_{x,}$ and CNF are around 5 ohm, demonstrating the low internal resistance for all the electrodes, benefiting from the desired electrical conductivity of MXene and carbon nanofibers (electrical conductivities were measured to be 1.29, 0.31, and 0.14 S m^{-1} for $Ti_3C_2T_x$/CNF6-2, $Ti_3C_2T_x$/CNF4-4, and $Ti_3C_2T_x$/CNF2-6 aerogels). The diameter of the semicircle indicates the resistance of ions migration and electron transfer at the interface of the electrode and electrolyte. Pure $Ti_3C_2T_x$ shows an unnoticeable semi-circle in this region, indicating the fast ion migration and electron transfer in MXene flakes, rendering an excellent electrochemical performance by $Ti_3C_2T_x$/CNF6-2 electrode. The cycling function of the $Ti_3C_2T_x$/CNF6-2 electrode was further evaluated at a current density of 1 A g^{-1} (Fig. 6F). Notably, the specific capacitance of $Ti_3C_2T_x$/CNF6-2 still retains 82.4% of its initial value after 8000 cycles, implying the great long-term stability of the $Ti_3C_2T_x$/CNF6-2 electrode.

In order to realize the feasibility of the assembled $Ti_3C_2T_x$/CNF composite aerogel, for energy-storage applications, a symmetric supercapacitor device was fabricated using the self-supported $Ti_3C_2T_x$/CNF6-2 aerogel as both positive and negative electrodes (denoted as $Ti_3C_2T_x$/CNF6-2//$Ti_3C_2T_x$/CNF6-2 SSC). Figure 7 A shows the obvious enlargement of the CV area, with the increase of the scan rate, the rectangular-shaped CV curves of the SSC in various scan rates (10, 20, 30, 50, 100 mV s^{-1}) suggest a favorable capacitive behavior in accordance with the results in three-electrode tests. Figure 7B presents the charge/discharge graph of the symmetric supercapacitor device with a typical symmetric configuration, the great linear relationship of time versus voltage demonstrates the perfect capacitive characteristic, ideal charge/discharge features, as well as great reversibility of the assembled SSC device. The specific capacitance and capacity based on the total mass of the two electrodes were calculated according to the GCD results using Eqs. (1) and (2). Remarkably, the $Ti_3C_2T_x$/CNF6-2//$Ti_3C_2T_x$/CNF6-2 SSC exhibit an impressive specific capacitance of 93.5 F g^{-1} (specific capacity of 56 C g^{-1}) at 1 A g^{-1}. In addition, the electrochemical cycle stability of the SSC device was studied. As shown in Fig. 7C, the capacitance retention rate of the $Ti_3C_2T_x$/CNF6-2//$Ti_3C_2T_x$/CNF6-2 SSC reaches above 95% after 5000 charge/discharge cycles at 10 A g^{-1}, and the charge/discharge curves before and after the cycling test exhibit inconspicuous difference, indicating the remarkable cycling stability of the SSC device. According to Eqs. (3) and (4), the energy density (E) and power density (P) of the $Ti_3C_2T_x$/CNF6-2//$Ti_3C_2T_x$/CNF6-2 SSC was further calculated. Ragone plots shown in Fig. 7D compiles the energy density and power density of the as-assembled SSC and other previously reported supercapacitor devices. Promisingly, $Ti_3C_2T_x$/CNF6-2//$Ti_3C_2T_x$/CNF6-2 SSC delivers a high energy density of 4.675 W h kg^{-1} at a power density of 300 W kg^{-1}, and still approaches an energy density of 3.425 W h kg^{-1} at a high power density of 6000 W kg^{-1}, which is better than that of some recently reported MXene related SSCs, such as M/G-5% (2.6 W h kg^{-1} at 80.3 W kg^{-1}) [28], BiOCl/MXene (6.2 W h kg^{-1} at 3756.8 W kg^{-1}) [29], MXene-N_2/H_2 (3.437 W h kg^{-1} at 700 W kg^{-1}) [30], Ti_2CT_{x}_Ar (2.19 W h kg^{-1} at 700 W kg^{-1}) [31], MXene/MoS_2 (5.1 W h kg^{-1} at 298 W kg^{-1}) [32], MXene/CNT (2.7 W h kg^{-1} at 311 W kg^{-1}) [33], graphene/MXene (5.7 W h kg^{-1} at 5000 W kg^{-1}) [34], and $Ti_3C_2T_x$-10 (4.7 W h kg^{-1} at 242 W kg^{-1}) [35]. This comparison proves the great potential of fabricated $Ti_3C_2T_x$/CNF composite aerogel in high-performance energy storage applications.

Conclusions

In summary, $Ti_3C_2T_x$/CNF composite aerogels, with "layer-strut" bracing 3D microscopic architecture were constructed by a gel–sol process, freeze-drying, and high-temperature carbonization treatments. 3D assembly of 2D $Ti_3C_2T_x$ flakes and 1D PAN short nanofibers was realized via the strong interfacial interaction between two building blocks. This configuration can effectively control restacking of few-layered $Ti_3C_2T_x$ flakes. As-fabricated $Ti_3C_2T_x$/CNF aerogels exhibit a highly ordered microporosity, with CNF pillars penetrating between lamellar MXene flakes, leading to the remarkable structural robustness and flexibility of the composite aerogels, as well as a convenient channel for electron transport and ion migration. As a result, fabricated $Ti_3C_2T_x$/CNF composite aerogel exhibited an outstanding gravimetric specific capacitance of 268 F g $^{-1}$ at a current density of 0.5 A g $^{-1}$ and excellent cycling stability up to 8000 cycles. Moreover, the symmetric supercapacitor device using the composite aerogel as both electrodes delivers a decent energy density of 3.425 W h kg^{-1} at 6000 W kg^{-1} together with excellent rate performance. This research provides a new route toward improving the electrochemical performance of MXene based energy storage materials.

Supplementary Information The online version contains supplementary material available at https://doi.org/10.1007/s42765-022-00140-z.

Acknowledgements This work is financially supported by the National Natural Science Foundation of China (No. 21875033), the Shanghai Scientific and Technological Innovation Project (No. 18JC1410600), the Program of the Shanghai Academic Research Leader (No. 17XD1400100), and the State Key Laboratory for Modification of Chemical Fibers and Polymer Materials (Donghua University).

Declarations

Conflict of interest There are no conflicts of interest to declare.

References

1. Xu T, Li X, Liang Z, Amar VS, Huang R, Shende RV, Fong H. Carbon nanofibrous sponge made from hydrothermally generated biochar and electrospun polymer nanofibers. *Adv Fiber Mater* **2020**;*2*:74.
2. Xue L, Fan W, Yu Y, Dong K, Liu C, Sun Y, Zhang C, Chen W, Lei R, Rong K, Wang Q. A novel strategy to fabricate core-sheath structure piezoelectric yarns for wearable energy harvesters. *Adv Fiber Mater* **2021**;*3*:239.
3. Liu S, Wan K, Zhang C, Liu T. Polyaniline-decorated 3D carbon porous network with excellent electrolyte wettability and high energy density for supercapacitors. *Compos Commun* **2021**;*24*:100610s.
4. Huang Z, Guo H, Zhang C. Assembly of 2D graphene sheets and 3D carbon nanospheres into flexible composite electrodes for high-performance supercapacitors. *Compos Commun* **2019**;*12*:117.
5. Tian J, Shi Y, Fan W, Liu T. Ditungsten carbide nanoparticles embedded in electrospun carbon nanofiber membranes as flexible and high-performance supercapacitor electrodes. *Compos Commun* **2019**;*12*:21.
6. Kunwar R, Krishnan SG, Misnon II, Zabihi F, Yang S, Yang C, Jose R. Transformation of supercapacitive charge storage behaviour in a multi elemental spinel $CuMn_2O_4$ nanofibers with alkaline and neutral electrolytes. *Adv Fiber Mater* **2021**;*3*:265.
7. Yu M, Wang Z, Liu J, Sun F, Yang P, Qiu J. A hierarchically porous and hydrophilic 3D nickel-iron/MXene electrode for accelerating oxygen and hydrogen evolution at high current densities. *Nano Energy* **2019**;*63*:103880.
8. Wang Q, Wang S, Guo X, Ruan L, Wei N, Ma Y, Li J, Wang M, Li W, Zeng W. MXene-reduced graphene oxide aerogel for aqueous zinc-ion hybrid supercapacitor with ultralong cycle life. *Adv Electron Mater* **2019**;*5*:1900537.
9. Wang Y, Wang X, Li X, Bai Y, Xiao H, Liu Y, Yuan G. Scalable fabrication of polyaniline nanodots decorated MXene film electrodes enabled by viscous functional inks for high-energy-density asymmetric supercapacitors. *Chem Eng J* **2021**;*405*:126664.
10. VahidMohammadi A, Moncada J, Chen H, Kayali E, Orangi J, Carrero CA, Beidaghi M. Thick and freestanding MXene/PANI pseudocapacitive electrodes with ultrahigh specific capacitance. *J Mater Chem A* **2018**;*6*:22123.
11. Zhao Q, Zhu Q, Miao J, Zhang P, Wan P, He L, Xu B. Flexible 3D porous MXene foam for high-performance lithium-ion batteries. *Small* **2019**;*15*:1904293.
12. Ming F, Liang H, Zhang W, Ming J, Lei Y, Emwas A, Alshareef HN. Porous MXenes enable high performance potassium ion capacitors. *Nano Energy* **2019**;*62*:853.
13. Zhou Z, Liu J, Zhang X, Tian D, Zhan Z, Lu C. Ultrathin MXene/calcium alginate aerogel film for high-performance electromagnetic interference shielding. *Adv Mater Interfaces* **2019**;*6*:1802040.
14. Li X, You W, Wang L, Liu J, Wu Z, Pei K, Li Y, Che R. Self-assembly magnetized MXene avoid dual-agglomeration with enhanced interfaces for strong microwave absorption through tunable electromagnetic property. *ACS Appl Mater Interfaces* **2019**;*11*:44536.
15. Ma Y, Yue Y, Zhang H, Cheng F, Zhao W, Rao J, Luo S, Wang J, Jiang X, Liu Z, Liu N, Gao Y. 3D synergistical MXene/reduced graphene oxide aerogel for a piezoresistive sensor. *ACS Nano* **2018**;*12*:3209.
16. Li R, Tian X, Wei M, Dong A, Pan X, He Y, Song X, Li H. Flexible pressure sensor based on cigarette filter and highly conductive MXene sheets. *Compos Commun* **2021**;*27*:100889.
17. Bu F, Zagho MM, Ibrahim Y, Ma B, Elzatahry A, Zhao D. Porous MXenes: synthesis, structures, and applications. *Nano Today* **2019**;*30*:100803.
18. Wang N, Wang H, Wang Y, Wei Y, Si J, Yuen ACY, Xie J, Yu B, Zhu S, Lu H, Yang W, Chan QN, Yeoh G. Robust, lightweight, hydrophobic, and fire-retarded polyimide/MXene aerogels for effective oil/water separation. *ACS Appl Mater Interfaces* **2019**;*11*:40512.
19. Li S, Li Y, Shao Y, Wang H. Emerging two-dimensional materials constructed nanofluidic fiber: properties, preparation and applications. *Adv Fiber Mater* **2021**. https://doi.org/10.1007/s42765-021-00111-w .
20. Hu M, Zhang H, Hu T, Fan B, Wang X, Li Z. Emerging 2D MXenes for supercapacitors: status, challenges and prospects. *Chem Soc Rev* **2020**;*49*:6666.
21. Song J, Guo X, Zhang J, Chen Y, Zhang C, Luo L, Wang F, Wang G. Rational design of free-standing 3D porous MXene/rGO hybrid aerogels as polysulfide reservoirs for high-energy lithium-sulfur batteries. *J Mater Chem A* **2019**;*7*:6507.
22. Qu L, Wang S, Yang X, Sun C. MXene/reduced graphene oxide hydrogel film extraction combined with gas chromatography-tandem mass spectrometry for the determination of 16 polycyclic aromatic hydrocarbons in river and tap water. *J Chromatogr A* **2019**;*1584*:24.
23. Yu C, Gong Y, Chen R, Zhang M, Zhou J, An J, Lv F, Guo S, Sun G. A solid-state fibriform supercapacitor boosted by host-guest hybridization between the carbon nanotube scaffold and MXene nanosheets. *Small* **2018**;*14*:1801203.
24. Li H, Chen R, Ali M, Lee H, Ko MJ. In situ grown MWCNTs/MXenes nanocomposites on carbon cloth for high-performance flexible supercapacitors. *Adv Funct Mater* **2020**;*30*:2002739.
25. Shang T, Lin Z, Qi C, Liu X, Li P, Tao Y, Wu Z, Li D, Simon P, Yang Q. 3D macroscopic architectures from self-assembled MXene hydrogels. *Adv Funct Mater* **2019**;*29*:1903960.
26. Zhang P, Zhu Q, Soomro RA, He S, Sun N, Qiao N, Xu B. In situ ice template approach to fabricate 3D flexible MXene film-based electrode for high performance supercapacitors. *Adv Funct Mater* **2020**;*30*:2000922.
27. Wang Y, Wang X, Li X, Bai Y, Xiao H, Liu Y, Liu R, Yuan G. Engineering 3D ion transport channels for flexible MXene films with superior capacitive performance. *Adv Funct Mater* **2019**;*29*:1900326.
28. Yan J, Ren CE, Maleski K, Hatter CB, Anasori B, Urbankowski P, Sarycheva A, Gogotsi Y. Flexible MXene/graphene films for ultrafast supercapacitors with outstanding volumetric capacitance. *Adv Funct Mater* **2017**;*27*:1701264.
29. Xia QX, Shinde NM, Yun JM, Zhang T, Mane RS, Mathur S, Kim KH. Bismuth oxychloride/MXene symmetric supercapacitor with high volumetric energy density. *Electrochim Acta* **2018**;*271*:351.
30. Rakhi RB, Ahmed B, Hedhili MN, Anjum DH, Alshareef HN. Effect of postetch annealing gas composition on the structural and electrochemical properties of Ti_2CT_x MXene electrodes for supercapacitor applications. *Chem Mater* **2015**;*27*:5314.
31. Rakhi RB, Ahmed B, Anjum D, Alshareef HN. Direct chemical synthesis of MnO_2 nanowhiskers on transition-metal carbide surfaces for supercapacitor spplications. *ACS Appl Mater Interfaces* **2016**;*8*:18806.
32. Hou W, Sun Y, Zhang Y, Wang T, Wu L, Du Y, Zhong W. Mixed-dimensional heterostructure of few-layer MXene based vertical aligned MoS_2 nanosheets for enhanced supercapacitor performance. *J Alloys Compd* **2021**;*859*:157797.

33. Yang L, Zheng W, Zhang P, Chen J, Tian WB, Zhang YM, Sun ZM. MXene/CNTs films prepared by electrophoretic deposition for supercapacitor electrodes. *J Electroanal Chem* **2018**;*830–831*:1.
34. Zhang L, Or SW. Self-assembled three-dimensional macroscopic graphene/MXene-based hydrogel as electrode for supercapacitor. *APL Mater* **2020**;*8*:91101.
35. Zhang X, Liu Y, Dong S, Yang J, Liu X. Flexible electrode based on multi-scaled MXene ($Ti_3C_2T_x$) for supercapacitors. *J Alloys Compd* **2019**;*790*:517.

Yongpeng Liu is a master's student in the School of Chemical and Material Engineering, Jiangnan University. He received the B.S. degree in chemical engineering and technology from Chongqing University in 2019. His research interests focus on the nanofiber assemblies for energy storage.

Dan Wang is currently a Master of the School of Chemical and Material Engineering, Jiangnan University. She joined Prof. Tianxi Liu's group in 2020 and her research interest focuses on the design and construction of functional fibers for diverse applications.

Chao Zhang is a professor of Donghua University. He received his PhD degree from Fudan University in 2013. His research interests include nano-/micro-fabrication of polymer composites for sensing and thermal management applications.

Yan Zhao received the Ph.D. degree in Materials Science at Fudan University in 2015. He joined the Institute of Energy Research, Jiangsu University, as an assistant professor in 2015 and became an associate professor in 2019. He joined the College of Chemistry and Chemical Engineering, Inner Mongolia University in 2022 as a professor. His research focuses on fiber-based and film-based nanodevices for wearable energy storage and conversion.

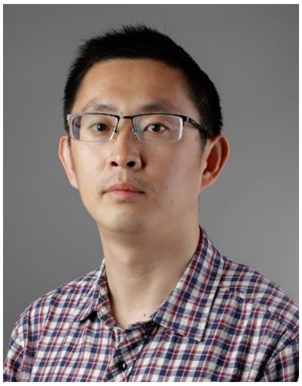

Piming Ma received his bachelor, master and PhD degrees from South China University of Technology, Shanghai Jiaotong University, and Eindhoven University of Technology, respectively, and is currently a full-time professor in Jiangnan University. He is the leader of research group of Bio-polymer and Composites, and an editorial board member of Polymer Degradation and Stability.

Weifu Dong received his Ph.D. degree from Beijing University of Chemical Technology in 2006. In 2007, he worked as a TU/e and DPI (the Netherlands) Postdoctoral Research Fellow. Since 2009, he has been a faculty member at School of Chemical and Material Engineering, Jiangnan University. His research interests include polymer nanocomposites, biodegradable and functional macromolecules.

Yunpeng Huang is currently an associate professor of the School of Chemical and Material Engineering, Jiangnan University. He received his PhD degree in polymer chemistry and physics from Fudan University in 2016. His research mainly focuses on the development of functional nanofibers and nanofiber composites.

Tianxi Liu is a professor of the School of Chemical and Material Engineering, Jiangnan University. He received his PhD degree from Changchun Institute of Applied Chemistry, Chinese Academy of Sciences in 1998. His research interests include polymer nanocomposites, polymer aerogel composites, nanofibers and their composites, new energy materials.